Strength, strain-rate sensitivity and ductility of copper with nanoscale twins

M. Dao [a], L. Lu [a,b], Y.F. Shen [b], S. Suresh [a,*]

[a] *Department of Materials Science and Engineering, Massachusetts Institute of Technology, 77 Massachusetts Avenue, Room 40140, Cambridge, MA 02139, USA*
[b] *Shenyang National Laboratory for Materials Science, Institute of Metal Research, Chinese Academy of Sciences, Shenyang 110016, China*

Abstract

We present a comprehensive computational analysis of the deformation of ultrafine crystalline pure Cu with nanoscale growth twins. This physically motivated model benefits from our experimental studies of the effects of the density of coherent nanotwins on the plastic deformation characteristics of Cu, and from post-deformation transmission electron microscopy investigations of dislocation structures in the twinned metal. The analysis accounts for high plastic anisotropy and rate sensitivity anisotropy by treating the twin boundary as an internal interface and allowing special slip geometry arrangements that involve soft and hard modes of deformation. This model correctly predicts the experimentally observed trends of the effects of twin density on flow strength, rate sensitivity of plastic flow and ductility, in addition to matching many of the quantitative details of plastic deformation reasonably well. The computational simulations also provide critical mechanistic insights into why the metal with nanoscale twins can provide the same level of yield strength, hardness and strain rate sensitivity as a nanostructured counterpart without twins (but of grain size comparable to the twin spacing of the twinned Cu). The analysis also offers some useful understanding of why the nanotwinned Cu with high strength does not lead to diminished ductility with structural refinement involving twins, whereas nanostructured Cu normally causes the ductility to be compromised at the expense of strength upon grain refinement.
© 2006 Acta Materialia Inc. Published by Elsevier Ltd. All rights reserved.

Keywords: Nanocrystalline materials; Nanoscale twins; Crystal plasticity; Copper; Computational model

1. Introduction

The strength, hardness, plastic deformation characteristics and ductility of metals and alloys are strongly dependent upon their micro- and nanoscale structural characteristics. Nanocrystalline (nc) metals and alloys, with average and entire range of grain sizes typically finer than 100 nm, are well known for their substantial high strength and generally much lower tensile ductility than their ultrafine crystalline (ufc) and microcrystalline (mc) counterparts, with grain sizes on the order of 100 nm–1 μm and greater than 1 μm, respectively [1–4].

Plastic deformation of conventional coarse-grained polycrystalline metals is mainly carried by lattice dislocations within individual grains. Refining grains by creating a higher concentration of grain boundaries (GBs) provides barriers to inter-grain dislocation motion, making the material harder to deform further, as suggested by the well-known Hall–Petch (H–P) relation [1,2,4]. When the grain size falls into the nanoscale regime, however, it becomes less favorable to activate lattice dislocation motion and the metal attains very high strength and hardness. Such nc metals often exhibit low tensile ductility at room temperature, which limits their practical applications. The tensile strain-to-failure of pure nc face-centered cubic (fcc) metals is typically smaller than a few per cent, and the region of the uniform deformation is even more limited [1,4]. Nanocrystalline metals also exhibit significantly higher

* Corresponding author. Tel.: +1 617 253 3320; fax: +1 617 253 0868.
E-mail address: ssuresh@mit.edu (S. Suresh).

sensitivity of plastic deformation to the rate of loading than ufc and mc metals [3–5].

Coherent twin boundaries (CTBs),[1] which are a special kind of boundary with low energy, serve as barriers to dislocation motion [6–8]. Recent studies on ufc-Cu (average grain size of 400–500 nm) indicates that at a fixed grain size, controlled introduction of nanoscale growth twins leads to an overall strengthening effect similar to that seen through grain refinement in the nanocrystalline regime, while maintaining appreciable ductility much higher than that normally obtained in nc-Cu [6–10]. Specifically, the flow stress, the sensitivity of flow stress to rate of loading, the activation volume and the hardness of ufc-Cu with nanoscale twins are found to be comparable to those of nc-Cu strengthened by grain refinement, when the nanoscale twin lamellar spacing in the former is comparable to the analogous grain size for the nc-Cu.

Atomistic simulations [11–13] suggest the possibility that intrinsic mechanisms of reduced ductility in nc metals arise from limited dislocation activity within the lattice and at GBs. Molecular dynamics simulations for deformation mechanisms across CTBs [14] as well as other binary coherent/semi-coherent interfaces [15–17] suggest that dislocations approaching CTBs can propagate into the adjacent twin grain by cross-slip at the boundary or combined with dissociation within the boundary plane [14]. Unfortunately, the current limitations of atomistic simulation in terms of relatively small specimen size and extremely high strain rate make it impractical to study with sufficient fidelity the macroscopic mechanical behavior including flow stress, strain hardening response and strain to failure in copper with nanoscale twins (nt-Cu). Our earlier continuum study invoked an idealized grain boundary affected zone (GBAZ) model for intercrystalline interfaces predicated upon von Mises plasticity characterization of intracrystalline deformation [3]. The model successfully captures some aspects of the deformation characteristics of nc metals. Nevertheless, it lacks the crystallographic details that are essential to describing the orientation-dependent deformation behavior of nanoscale twins including shearing parallel and across the twin boundaries (TBs). The model proposed by Asaro and Suresh [9] provides insights into how defect nucleation and motion at boundaries influence the mechanistic processes leading to elevated strength, enhanced strain-rate sensitivity to plastic flow and diminished activation volume in fcc metals with nc grains and nanoscale twins. However, it does not provide a fully quantitative description of the stress–strain characteristics and ductility of nc- and nt-Cu.

In order to overcome the limitations of these earlier approaches, we have developed a detailed computational framework, motivated by a systematic experimental program and comprehensive electron microscopy observations. This framework provides a basis with which to model the

crystallographic anisotropy of intracrystalline deformation as well as soft and hard modes of deformation along and across TBs in Cu with nanoscale growth twins. The model comprises a sufficiently large sample, or unit cell, of GBs and TBs, and provides quantitative predictions of the full stress–strain characteristics. In addition, the model facilitates quantitative estimates of the tensile ductility by recourse to a physically motivated failure criterion. These predictions are compared with experimental observations of three different specimens in which the twin spacing is systematically varied from about 15–100 nm, while the grain size of the ufc-Cu is held fixed. In an attempt to develop a comprehensive basis for validating different predictive capabilities of the model with real material behavior, we report in this paper new experimental results conducted on nt-Cu. In addition, we provide a detailed summary of our earlier work and other related prior work on nc-Cu from a variety of processing routes and mechanical testing methods. These observations on mechanical deformation characteristics are supplemented with new transmission electron microscopy (TEM) observations of the as-processed and post-deformed samples to identify defect interactions with GBs and TBs. These TEM observations, in turn, guide some of the mechanistic processes modeled in the computational simulations. The model also introduces straightforward relationships of nanoscale size effects by examining the effects of twin spacing on flow stress, strain-rate sensitivity and ductility at the crystalline level. The assembled polycrystal aggregate consists of randomly oriented, twin-comprising crystals, where strain compatibility and stress continuity across the grain boundaries are both preserved within the model framework during the entire deformation process. With the quantitative understanding of the macroscopic properties available from this framework, possible processing routes could be explored for optimization of structural features (such as the twin geometry and density) that yield desirable combinations of strength and ductility.

The plan of the paper is as follows. In Section 2, we review available experimental observations for nc- and nt-Cu in order to develop the necessary perspective with which to examine the computational framework and analysis. The computational setup and constitutive models are described in detail in Section 3. Computational results follow in Section 4. Discussions of key parameters influencing the plastic deformation response of nt-Cu are given in Section 5. A brief summary of key findings follows in Section 6.

2. Experimental observations

2.1. Summary of uniaxial tensile test results

Uniaxial tensile tests at constant strain rates of 6×10^{-4}–6×10^{-1} s^{-1} have been performed on three nt-Cu specimens with different twin densities (referred to as nt-Cu-fine, nt-Cu-medium and nt-Cu-coarse) that were synthesized by means of pulsed electrodeposition (PED) technique at room temperature (RT). These experimental results are

---

[1] Unless stated otherwise, throughout this paper the term twin boundaries refers to coherent twin boundaries.

either from prior work (for the fine and coarse twin structures [6]) or from new results (for the medium twin structure) obtained in this study. Statistical analysis of the spacing of nanotwins along the [1 1 0] direction from the TEM observation show that the average twin spacing is about 15 nm for nt-Cu-fine sample, and about 35 and 100 nm for nt-Cu-medium and nt-Cu-coarse, respectively. From TEM observations and statistical measurements of twins, it is found that only one twin variant is observed within each grain in the as-deposited Cu specimen in most cases. From these measurements, the probability of only one twin variant occurring in the as-deposited nt-Cu is estimated to be more than 95%. It is therefore reasonable to assume in the computational model that each twin-comprising grain contains only one twin variant. To better understand the influence of TBs on mechanical behavior, the ufc-Cu without twins, but having essentially the same average grain size prepared by direct current (DC) electrodeposition from the same solution, is selected for comparison (referred to as ufc-Cu-control). Note that all four Cu specimens examined in this paper have the similar average grain size of approximately 400–500 nm. Further details on specimen preparation methods, microstructure characterization and mechanical testing of the specimens can be found elsewhere [7,8].

Fig. 1 shows the variation of true stress as a function of true strain for the four specimens deformed in uniaxial tension. Table 1 provides a detailed quantitative summary of the experimental results for all the tensile tests and includes details of grain size, twin spacing, yield strength, tensile strength, strain at tensile strength and tensile strain to failure. Also included are the strain rate sensitivity exponent, m, determined at different strain rates from the uniaxial tensile tests and strain rate jump tests [9]. A clear effect of twin spacing on the mechanical properties is evident from these results. There are three distinctive trends in terms of twin lamellar spacing:

1. The yield strength and tensile strength increase with decreasing twin spacing.
2. The ductility increases significantly with decreasing twin spacing.
3. When the strain-rate is increased by several orders of magnitude, a significant strain-rate sensitivity is detected in the Cu with nano-sized twins, and the rate sensitivity exponent m (defined in the footnote to Table 1) increases significantly with decreasing twin spacing.

For nt-Cu-coarse, the yield strength is close to 500 MPa and quite limited ductility (about 3%) is obtained from tensile tests. However, for nt-Cu-fine, the yield strength is close to 900 MPa, which is about 4.5 times higher than that of ufc-Cu-control with about the same grain size, but the ductility is comparable at 13–16%.

As noted earlier, the increase in strength, hardness and strain-rate sensitivity of deformation caused by the introduction of nanoscale twins mirrors that observed in Cu when the grain size is refined to the nanoscale dimensions. However, enhancements in strength with the introduction of nanoscale growth twins in ufc-Cu occurs without any concomitant reduction in ductility. In the case of grain refinement, by contrast, the reduction in the structural feature size into the nanometer regime leads to a significant reduction in ductility, as summarized in Table 2 from the available results for polycrystalline Cu (from Refs. [7,10,18–25]).

2.2. Post-deformation microstructure observation

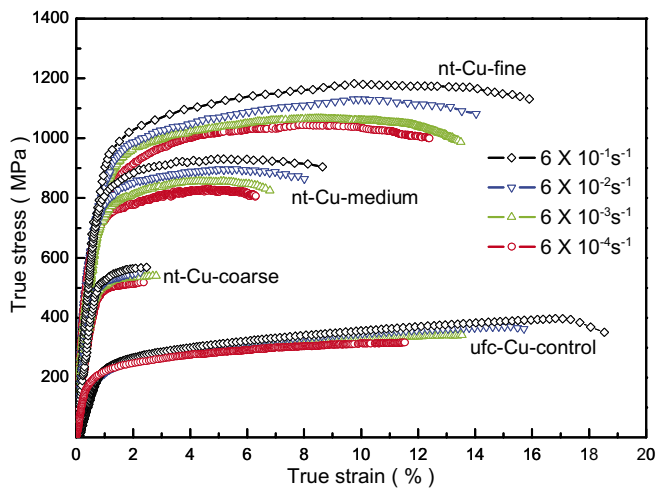The post-tensile TEM microstructure observations suggest that the interaction of dislocations with TBs plays a

Fig. 1. Tensile stress–strain curves of as-deposited nt-Cu specimens tested at different strain-rates (as indicated) at room temperature. The average grain size and twin spacing of the specimens are listed in Table 1.

Table 1
Summary of microstructure characteristics, such as grain size and twin lamellar spacing, and mechanical properties, such as yield strength (σ_y), tensile strength (σ_{ts}), ductility (ε (%)) and strain rate sensitivity exponent (m), of the nt-Cu samples and ufc-Cu-control from the tensile tests at a constant strain rate of 6×10^{-3} s^{-1}

Sample	Grain size (nm)	Twin spacing (nm)	σ_y (MPa)	σ_{ts} (MPa)	ε (%)		m (uniaxial tensile test)[a]	m (tensile strain-rate jump test [9])
					ε_{ts}	$\varepsilon_{failure}$		
nt-Cu-fine	400 ± 20	15 ± 5	857 ± 50	1118	11.6	14	0.037 ± 0.014	0.035–0.046
nt-Cu-medium	450 ± 20	35 ± 10	701 ± 50	897	5.6	8.0	0.026 ± 0.012	–
nt-Cu-coarse	425 ± 20	100 ± 20	488 ± 30	552	2.2	2.2	0.012 ± 0.010	0.015–0.020
ufc-Cu-control	400 ± 20	–	198 ± 10	371	15.2	15.7	0.005 ± 0.001	0.005

[a] The strain rate sensitivity exponent m is defined as [17] $m = \frac{\partial \ln \sigma}{\partial \ln \dot{\varepsilon}}\big|_{\varepsilon,T}$, where σ is the flow stress and $\dot{\varepsilon}$ is the strain rate.

Table 2
Summary of experimental results on the effects of structural size on mechanical response and activation volume of polycrystalline Cu (m is the strain rate sensitivity exponent, σ_y is yield strength, $\varepsilon_{failure}$ is elongation-to-failure from tension tests, v^* is estimated activation volume)

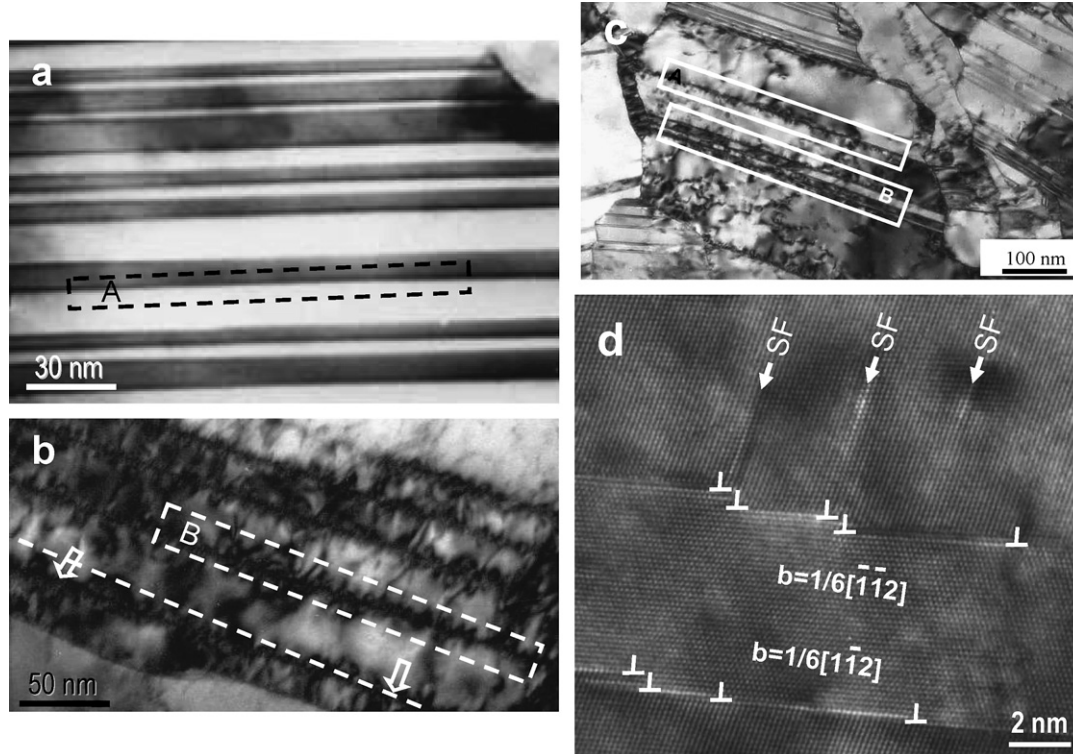| Material	Grain size (twin spacing)	Strain (or loading) rate range	m	σ_y (MPa)	$\varepsilon_{failure}$ (%)	v^*	Test method used	Reference
ufc-Cu (essentially no twins)	500 nm	10^{-5}–10-2 s^{-1}	~0.005	~200	>20%	~$135b^3$	Tensile strain rate up-jump test	[10]
ufc-Cu (lower twin density)	500 nm (~100 nm)	10^{-5}–10^{-2} s^{-1}	0.020–0.015	~500	~3%	–	Tensile strain rate up-jump test	[10]
ufc-Cu (higher twin density)	500 nm (~5 nm)	10^{-5}–10^{-2} s^{-1}	0.0046–0.035	~870	~14%	–	Tensile strain rate up-jump test	[10]
ufc-Cu (essentially no twins)	500 nm	10^{-5}–10^{-2} s^{-1}	0.005 ± 0.001	~500	>20%	~$135b^3$	Tensile test	[7]
ufc-Cu (lower twin density)	500 nm (~90 nm)	0.1–100 mN/s	0.025 ± 0.009	570–640	–	~$22b^3$	Nanoindentation	[7]
ufc-Cu (higher twin density)	500 nm (~20 nm)	0.1–100 mN/s	0.036 ± 0.009	660–900	–	~$12b^3$	Nanoindentation	[7]
Cold-deformed ufc-Cu	300 nm	6×10^{-7}–10^{-4} s^{-1}	0.026–0.009	370	<6%	~$48b^3$	Tensile jump test	[18]
ECAP+cold-rolled ufc-Cu	300 nm	6×10^{-7}–10^{-4} s^{-1}	0.019	~400	~7%	~$41b^3$	Tensile jump test	[19]
Cold-deformed ufc-Cu	200 nm		0.015	~450	~7%	~$48b^3$	Tensile jump test	[19]
ECAP ufc-Cu (12 passes)	200–300 nm	10^{-4}–10^{-2} s^{-1}	0.017–0.023	346	>35%	$60 \sim 100b^3$	Compression jump test	[20]
LTMS-Cu	10 ± 5 nm	10^{-3}–10^{-2} s^{-1}	0.06 ± 0.01	~1000	–	$8 \pm 2b^3$	Nanoindentation	[21]
RTMS-Cu	31 ± 12 nm	10^{-3}–10^{-2} s^{-1}	0.038 ± 0.006	~650	–	$18 \pm 4b^3$	Nanoindentation	[21]
SAMT Cu	42 ± 15 nm	10^{-3}–10^{-2} s^{-1}	0.032 ± 0.003	~580	–	$23 \pm 3b^3$	Nanoindentation	[21]
ECAP Cu	190 ± 80 nm	10^{-3}–10^{-5} s^{-1}	0.020 ± 0.007	~557	–	$46 \pm 23b^3$	Nanoindentation	[21]
BM nc-Cu	54 nm	10^{-6}–10^{-4} s^{-1}	0.026	688	~3%	$25b^3$	Tensile jump test	[22]
mc Cu	12–90 μm		0.007–0.004			$1000b^3$	Tensile test	[23]
mc Cu	40 μm		0.006			–	–	[24,25]

Fig. 2. TEM observations of nt-Cu specimens. (a) Before deformation, the TBs are straight and no dislocations are observed. (b) nt-Cu-fine after tensile test showing dislocation pile ups along TBs and curved TBs; a region within a few nanometers of a TB is often heavily influenced by the dislocations along the TBs. (c) nt-Cu-coarse after tensile test again showing dislocation pile ups along TBs. White rectangle A shows a TB with large twin spacing and white rectangle B shows a few TBs with smaller twin spacing. Again a region within a few nanometers of a TB is often heavily influenced by the dislocations along the TBs. (d) High resolution TEM (HRTEM) of a nt-Cu-fine sample, showing partial dislocation disassociation, dislocation pile up and TB bending. See text for more details.

crucial role in the plastic deformation for the nt-Cu. Abundant dislocation debris is seen in the vicinity of TBs/GBs in nt-Cu-fine, as shown in Fig. 8 of Ref. [7]. Compared to the relatively defect-free microstructure of as-deposited nt-Cu-fine (Fig. 2(a)), the typical structure of the deformed specimen is populated with a high density of dislocations (Fig. 2(b)). TBs with copious dislocations and debris are not as clear, sharp and straight as the original coherent TBs in the as-deposited condition (see the black rectangle A in Fig. 2(a)), whereas stepped (the arrows in Fig. 2(b)) or even curved TBs (see the white rectangle B in Fig. 2(b)) are frequently seen. These curved TBs indicate that relative rotation of the order of 10–15° is common within the post-mortem microstructure. It is clearly observed that in Fig. 2(b) and (c) (for nt-Cu-fine and nt-Cu-coarse, respectively), within a few nm of the TBs, the crystal lattice is often elastically strained due to the high density of the dislocation debris accumulated along the TBs during deformation. High resolution TEM (HRTEM) observation shows that a high density of dislocation debris, identified as Shockley partial dislocations, are deposited along TBs in nt-Cu-fine, as shown in Fig. 2(d).[2] The spacing between two adjacent partial dislocations is only 1 or 2 nm. The accumulation of the dislocation debris appears to result in curved TBs as clearly seen in Fig. 2(d).

The comparison of TEM observations before and after deformation suggests that most of the plastic strain is carried by the dislocations piling up along the TBs, which results in shear strain accumulation at the TBs (note that a TB is an fcc slip plane). TBs are likely to take on much more strain than the internal volume residing beyond a few nanometers away from the TBs. The steps observed in the deformed TBs (Fig. 2(d)) and our earlier TEM observations [8] suggest that dislocations also propagate across initially coherent TBs, in addition to dislocations accumulating within the TBs. In addition, as discussed by Mahajan and Chin [26] for cobalt–iron alloys, in the review by Christian and Mahajan [6] and more recently by Jin et al. [14], dislocations gliding on a {1 1 1} plane can cross slip onto an equivalent plane in the twin, move across the twin and exit from the second TB. Therefore, analyses of plastic deformation characteristics of nt-Cu must inevitably account for both the crystallographic anisotropy and inhomogeneous straining, in order to describe accurately the constitutive behavior. The present analysis was motivated by these observations and requirements.

_____

[2] In order to determine the Burgers vector of the trapped dislocation at coherent TBs, the local Burgers circuit method was employed. First, selected area diffraction pattern confirmed that zone axis is along ⟨1 1 0⟩ direction. Second, an atom-by-atom path was taken around the trapped dislocation to form a closed loop. Next, the same atom-to-atom sequence was made in a dislocation-free area, where the circuit did not close. The vector required to complete the circuit, i.e., the closure failure, is the projected Burgers vector of the trapped dislocation. Crystallographic analysis using the Thompson tetrahedral shows that the closure failure is consistent with a partial dislocation with Burgers vector of $1/6\langle 1 1 2\rangle$ type. Further details of the TEM methods employed can be found in Ref. [8].

3. Model setup

3.1. The TB-affected zone (TBAZ)

In an earlier study, a model for the GBAZ (schematically shown in Fig. 8 in Ref. [3]) was proposed to understand the grain-size-dependence and rate-dependent deformation and failure of nanostructured materials [3]. The GBAZ model was mainly motivated by TEM observations and atomistic simulations. In the HRTEM studies by Kumar et al. [27], the GBs of high-purity electrodeposited nc Ni were found to be atomically sharp and no amorphous phase was present at the grain-boundary regions. The in situ TEM study [27] observed dislocation activities within grain boundaries at grain sizes as low as 30 nm for the same nc Ni sample. On the other hand, atomistic simulations of mechanical deformation of nc-Cu [11,13] and nc-Ni [12] suggest that grain-boundary atoms as well as atoms up to 7–10 lattice parameters away from the grain boundary are heavily involved in plastic deformation. Deformation was mostly taken up by atoms at and nearby grain boundaries. Those simulation results suggest that the material near grain boundaries is easier to deform and that the associated deformation mechanisms are likely to be rate sensitive [11–13]. The concept of a GBAZ thus refers to a region adjoining the grain boundaries in nc metals where the crystalline lattice is elastically strained. Atoms within this GBAZ are more likely to be involved in the plastic deformation process. Assuming that the GBAZ is plastically much softer than the theoretical strength, and that the GBAZ deforms at a relatively higher rate sensitivity than the grain interior, the model correctly captured the size and rate-dependent deformation behavior of nc-Ni [3].

Motivated by the TEM observations in Fig. 2 of the current paper, a TBAZ model is proposed, where each TB is considered as a special GB with a high aspect ratio in terms of the grain shape and mirrored slip geometries between adjacent twin lamellae. Another important aspect of the nt-Cu TB is that it lies on a {1 1 1} plane that contains three {1 1 1}⟨1 1 0⟩ slip systems. The concept of a TBAZ refers to the region adjoining the TBs where the crystalline lattice is elastically strained although no obvious lattice defects are observed prior to plastic deformation. Similar to the GBAZ model, each of the TBs may be treated as a special GB, where the plastic deformation in the nt-Cu is concentrated in the vicinity of TBs. The TBAZ model assumes that dislocation-based activities in the vicinity of TBs are the dominant plastic deformation mechanism for the nt-Cu. The following assumptions are made with the TBAZ model (Fig. 3):

1. A TBAZ within the nanoscale twin lamellae spans of the order of about 7–10 lattice parameters away from the TB, which is on the same order as a GBAZ.
2. The TBAZ is plastically softer than the predominantly elastic crystal interior region between TBAZs.
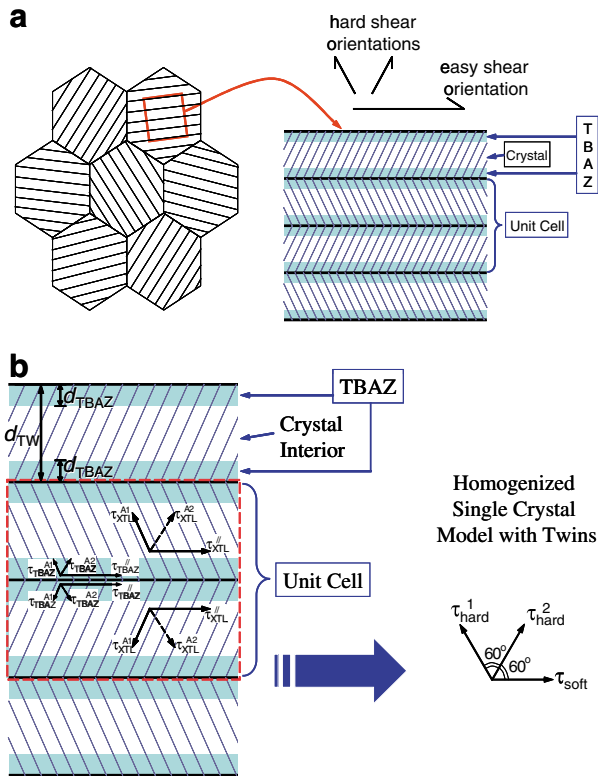
Fig. 3. Schematic drawings of the proposed twin boundary affected zone (TBAZ) model. (a) TBAZ refers to the region adjoining the twin boundaries where the crystalline lattice is elastically strained. (b) Homogenized nanoscale twin containing single crystal model. See text for more details.

3. There is a significant plastic anisotropy between the shear deformation parallel to the TBs and the shear deformation across the TBs.
4. The TBAZ deforms with a relatively larger rate sensitivity than the crystal interior region.

The first two assumptions are directly motivated by experimental observations (Fig. 2(a)–(c)) which reveal that the TBs, on either side, are populated with a region of softer material with a high dislocation density (with respect to the perfect crystal). Fig. 2(b) and (c) reveals that the thickness of this region is approximately the same for the nt-Cu-fine and nt-Cu-coarse. This observation is consistent with mechanistic models [9] and MD simulations [14], which suggest a much smaller localized activation volume and consequently higher rate sensitivity for the related deformation processes with nanoscale twins.

Considering the inherently two-dimensional characteristic of the twin lamellae, in which the length scale parallel to

the TBs (of the order of hundreds of nanometers) is significantly larger than that perpendicular to the TBs (on the order of tens of nanometers), it is expected that there exists a significant plastic anisotropy where the shear deformation parallel to the TBs is relatively easier (easy shear orientation or soft mode) and the shear deformation across the TBs is considerably harder (hard shear orientation or hard mode).

Due to the small distance between adjacent TBs, a TBAZ that spans 7–10 lattice parameters in thickness measured from TB can occupy a significant total volume fraction of the sample. Table 3 tabulates the TBAZ vol.% versus twin spacing. It is noted that the TBAZ thickness should be closely related to the characteristic dislocation core size and dislocation stress field for dislocations piling up along TBs. The TBAZ thickness, however, would change slightly with strain accumulation due to the overlapping stress fields of individual dislocations. Assuming the TBAZ to be of the order of 10 lattice parameters in thickness, the TBAZ region occupies 48 vol.% at a twin spacing of 15 nm, 36 vol.% at 20 nm twin spacing, 20.6 vol.% at 35 nm twin spacing and 7.2 vol.% at 100 nm twin spacing.

3.2. A homogenized single crystal model with twins

The three-dimensional slip geometry of nt-Cu is idealized with a two-dimensional model here while preserving the most important plastic deformation characteristics. It is worth noting here that two-dimensional crystal plasticity idealization of actual three-dimensional geometries has also been successfully used previously to study the deformation processes and failure modes in lamellar TiAl [28,29] as well as for single crystalline and micrograined polycrystalline fcc metals [30,31].

Dividing each twin lamella into the TBAZ region and the crystal interior region, and accounting for all the lamellae in detail, would be computationally expensive and theoretically cumbersome. For example, in Fig. 3(b), the idealized two-dimensional single crystal containing the nanotwins would have two regions with different constitutive laws describing the deformation behavior. In both the TBAZ region and the crystal interior region, the shear strength of a slip system parallel to the TBs would be different from the shear strength of slip systems with slip planes oriented at different angles with respect to the TBs. In addition, the shear strength values in the TBAZ region would also be different from those in the crystal interior region. Similarly, different treatments of the rate sensitivity need to be considered as well.

Table 3
Estimation of twin boundary affected zone (TBAZ) volume percentage for nt-Cu (the lattice spacing for Cu at room temperature is 3.6 Å)

Twin spacing (nm)	15	20	30	35	40	75	90	100
TBAZ vol.% (7 lattice parameter)	33.6	25.2	16.8	14.4	12.6	6.7	5.6	5.0
TBAZ vol.% (10 lattice parameter)	48.0	36.0	24.0	20.6	18.0	9.6	8.0	7.2

Taking into account of the most prominent deformation characteristics, a homogenized single crystal constitutive model is proposed here. This model is schematically illustrated in Fig. 3(b). The shear deformation along the TBs is modeled using a soft mode slip system, where the critical resolved shear stress, τ_{soft}, is taken to be the volume-averaged value of its counterparts in both the TBAZ and crystal interior regions; this value is mainly determined by the grain size and is estimated to be of the same order as the critical resolved shear stress of ufc-Cu with the same grain size. The strain rate sensitivity of the soft mode slip system (m_{soft}) is taken as the volume average of the crystal interior region (assumed to be the same as that of ufc-Cu with a similar grain size) and the TBAZ region (for which a much higher rate sensitivity is prescribed). The shear deformation across the TBs is modeled using two hard mode slip systems, representing the alternating mirrored slip geometries across the TBs. The critical resolved shear stresses of the two hard modes, τ_{hard}^1 and τ_{hard}^2, are again taken as volume-averaged values of their counterparts in both the TBAZ and crystal interior regions; these values are primarily determined by the twin spacing. Similar treatments of the rate sensitivity are assumed for the hard mode slip system.

3.3. Single crystal constitutive model and numerical implementation

A rate-dependent crystal plasticity constitutive theory is used in this study. The theory is modified from the earlier versions [28–32], where the primary focus was deformation of microcrystalline metals and alloys. The deformation of a single crystal from the reference configuration to the deformed configuration can be decomposed into plastic shearing on the one hand, and elastic stretching and lattice rotation, on the other. The deformation gradient, $\mathbf{F}$, is thus decomposed as

$$\mathbf{F} = \mathbf{F}^* \cdot \mathbf{F}^P, \tag{1}$$

where $\mathbf{F}^P$ is the plastic deformation gradient which represents the shear flow of crystal through the undeformed lattice along various slip systems, and $\mathbf{F}^*$ is the elastic deformation gradient representing the elastic stretching and rigid body rotation of the crystal.

The velocity gradient of the single crystal is given as

$$\mathbf{L} = \dot{\mathbf{F}} \cdot \mathbf{F}^{-1}. \tag{2}$$

The plastic part of the velocity gradient is taken to be the summation of the plastic shear flow over all slip systems as

$$\dot{\mathbf{F}}^P \cdot \mathbf{F}^{P-1} = \sum_\alpha \dot{\gamma}_\alpha \mathbf{s}_\alpha \mathbf{m}_\alpha, \tag{3}$$

where $\dot{\gamma}_\alpha$ is the shear rate on the αth slip system of which the αth slip system is defined by its slip direction $\mathbf{s}_\alpha$ and its slip plane normal $\mathbf{m}_\alpha$. The resolved shear stress of the slip system α, τ_α, is defined as

$$\tau_\alpha = \mathbf{m}_\alpha^* \cdot \boldsymbol{\tau} \cdot \mathbf{s}_\alpha^*, \tag{4}$$

where

$$\mathbf{s}_\alpha^* = \mathbf{F}^* \cdot \mathbf{s}_\alpha; \quad \mathbf{m}_\alpha^* = \mathbf{m}_\alpha \cdot \mathbf{F}^*; \quad \boldsymbol{\tau} = J\boldsymbol{\sigma} \tag{5}$$

in which $J = \det \mathbf{F}$ is the Jacobian, $\boldsymbol{\tau}$ is the Kirchhoff stress tensor, $\boldsymbol{\sigma}$ is the Cauchy stress tensor, $\mathbf{s}_\alpha^*$ is along the αth slip direction in the deformed configuration, and $\mathbf{m}_\alpha^*$ is normal to the αth slip plane in the deformed configuration. The shear rate on the slip system α, $\dot{\gamma}_\alpha$, in Eq. (3) is a standard power law flow rule

$$\dot{\gamma}_\alpha = \dot{\gamma}_0 \, \text{sgn}\{\tau_\alpha\} \left\{ \left| \frac{\tau_\alpha}{g_\alpha} \right| \right\}^{\frac{1}{m_\alpha}}, \tag{6}$$

where τ_α is the current value of resolved shear stress, $g_\alpha > 0$ is the current value of slip resistance, m_α is the material rate sensitivity exponent of slip system α, and $\dot{\gamma}_0$ is a reference shear strain rate.

The slip resistance g_α of the αth slip system is obtained by the path-dependent integration of the evolution equation

$$\dot{g}_\alpha = \sum_\beta h_{\alpha\beta}(\gamma_a)|\dot{\gamma}_\beta|, \quad \gamma_a = \int_0^t \sum_\alpha |\dot{\gamma}_\alpha| \, \mathrm{d}t, \tag{7}$$

where $h_{\alpha\beta}$ is a matrix of hardening moduli, and γ_a is the accumulated sum of slips. The initial conditions for this evolution are given by $g_\alpha = g_\alpha(\gamma_a = 0) = g_\alpha^0$. The specific form of the hardening matrix is taken as

$$h_{\alpha\beta} = qh + (1 - q)h\delta_{\alpha\beta}, \tag{8}$$

where q sets the level of latent hardening to the self hardening of the slip system, and h is the self-hardening rate. Other forms of latent hardening relations may be used [33,34], while the model predictions are reasonably close to the experimentally observed yield surfaces [35].

The single crystal's linear elasticity can be defined as

$$\dot{\mathbf{S}}^* = \mathbf{K} : \dot{\mathbf{E}}^*, \tag{9}$$

where $\mathbf{S}^* = \mathbf{F}^{*-1} \cdot \boldsymbol{\tau} \cdot \mathbf{F}^{*-T}$ is the lattice-based second Piola–Kirchhoff stress, $\mathbf{E}^* = (\mathbf{F}^{*T} \cdot \mathbf{F}^* - \mathbf{I})/2$ is the Green strain of the lattice, and $\mathbf{I}$ is the second-order identity tensor. The final constitutive theory is then expressed in terms of the second Piola–Kirchhoff stress, $\mathbf{S} = \mathbf{F}^{-1} \cdot \boldsymbol{\tau} \cdot \mathbf{F}^{-T}$, and the Green strain, $\mathbf{E} = (\mathbf{F}^T \cdot \mathbf{F} - \mathbf{I})/2$. Manipulation of the above equations gives the rate form of the final constitutive equation

$$\dot{\mathbf{S}} = \mathbf{L} : \dot{\mathbf{E}} - \sum_\alpha \dot{\gamma}_\alpha \mathbf{X}_\alpha, \tag{10}$$

where

$$
\begin{aligned}
L_{ijrn} &= \sum_k \sum_l \sum_p \sum_q F_{ik}^{P-1} F_{jl}^{P-1} K_{klpq} F_{rp}^{P-1} F_{nq}^{P-1}, \\
\mathbf{X}_\alpha &= \mathbf{F}^{P-1} \cdot \{\mathbf{K} : \mathbf{A}_\alpha + 2\mathbf{H}_\alpha\} \cdot \mathbf{F}^{P-T}, \\
\mathbf{A}_\alpha &= \text{sym}\{\mathbf{F}^{*T} \cdot \mathbf{F}^* \cdot (\mathbf{s}_\alpha \mathbf{m}_\alpha)\}, \\
\mathbf{H}_\alpha &= \text{sym}\{(\mathbf{s}_\alpha \mathbf{m}_\alpha) \cdot \mathbf{S}^*\},
\end{aligned} \tag{11}
$$

with sym$\{\cdot\}$ denotes the symmetric part of $\{\cdot\}$. Details of the development of Eqs. (10) and (11) can be found elsewhere [32,36] and are therefore omitted here. The crystal
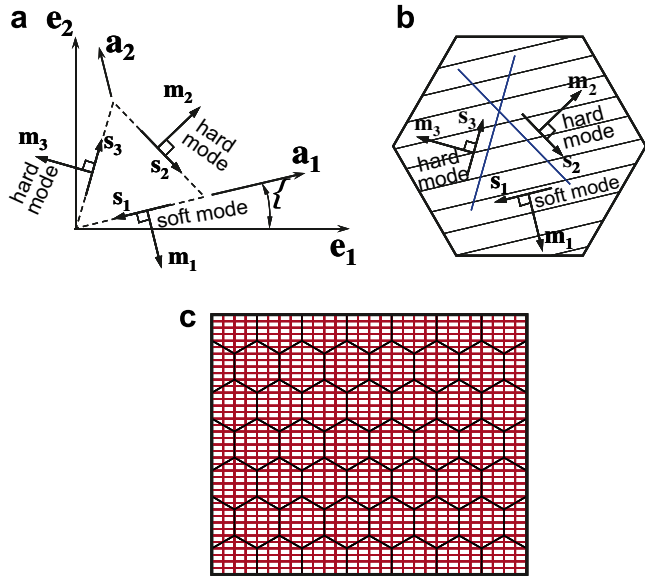
Fig. 4. Polycrystal model setup. (a) Arrangement of the single crystal slip systems. Angle ψ represents the angle between the lab axes $\mathbf{e}_1$–$\mathbf{e}_2$ and the local axes $\mathbf{a}_1$–$\mathbf{a}_2$. (b) Model single crystal with TB orientation marked with parallel lines. (c) Finite element mesh containing 52 grains, where the orientation of each grain is randomly generated.

plasticity model is implemented using the algorithms defined in [31,32].

3.4. Polycrystal assembly

Fig. 4 shows the polycrystal assembly containing 52 grains, where each grain follows the homogenized crystalline model described earlier. Periodic boundary conditions are enforced along the four sides. The finite element mesh includes 5000 elements of four-node, iso-parametric quadrilaterals with reduced integration on the pressure. The mesh is continuous across grain boundaries where grain boundary sliding is not allowed. The mesh is subjected to a uniaxial tension boundary condition. The orientation of each constituent grain in the model microstructure is randomly generated.

4. Results

Material parameters are selected to study the tensile experiments shown in Fig. 1 and Table 1. A simple power law hardening law is assumed for both soft mode and hard mode slip systems

$$g_\alpha(\gamma_a) = g_\alpha^0 \left(1 + \frac{G}{g_\alpha^0}\gamma_a\right)^{n_\alpha}, \tag{12}$$

where G is the shear modulus, and n_α is the strain hardening exponent of the αth slip system. The self-hardening rate is simply given by

$$h_{\alpha\alpha}(\gamma_a) = \frac{\partial g_\alpha(\gamma_a)}{\partial \gamma_a}. \tag{13}$$

Considering that the latent hardening effect is taken into account using the accumulated sum of slips, γ_a, as defined in Eq. (7), the off-diagonal hardening matrix components are set to zero, i.e., $h_{\alpha\beta} = 0$ when $\alpha \neq \beta$. For the slip system parallel to the TBs, the soft mode critical resolved shear stress is chosen to be the same as that of ufc-Cu-control,

$$g_1^0 = \tau_{\text{CRSS}} \text{ (soft mode)} = \sigma_y(d_{\text{GS}})/3 = 200 \text{ MPa}/3$$
$$= 67 \text{ MPa}, \tag{14}$$

where for the grain size $d_{\text{GS}} = 400$–450 nm, the tensile yield strength is measured to be around 200 MPa, and the Taylor factor is taken as 3. The strain hardening exponent is given as $n_1 = n$ (soft mode) $= 0.3$, which reflects the relatively large strain hardening exhibited by ufc-Cu-control. For the hard mode slip systems, assuming that the critical resolved shear stress approximately scales with the twin lamellar spacing, d_{TWIN}, via the classical H–P-type relationship beyond a certain critical length scale,

$$g_2^0 = g_3^0 = \tau_{\text{CRSS}} \text{ (hard mode)}$$
$$\approx \tau_{\text{th}} \left(\frac{d_{\text{th}}}{d_{\text{TWIN}}}\right)^{\frac{1}{2}} \quad \text{when } d_{\text{TWIN}} > d_{\text{th}}, \tag{15}$$

where d_{TWIN} is the twin spacing, d_{th} is the critical twin spacing below which there would be no dislocation pile-up inside the twins, resulting in a critical shear strength on the order of the theoretical strength. Here τ_{th} represents the magnitude of the theoretical strength when the size scale is extremely small. In the simulations, we take $d_{\text{th}} = 13$ nm and $\tau_{\text{th}} = 1$ GPa. A zero strain hardening exponent is assumed here with $n_2 = n_3 = n$ (hard mode) $= 0$, which reflects low or no strain hardening generally observed with nanocrystalline materials.

For the rate sensitivity, the average value of m for both hard and soft modes of deformation is simply taken as the volume average of the TBAZ and the crystal interior regions

$$m = m_1 = m_2 = m_3 = (1 - f_{\text{TBAZ}})m_{\text{XTL}} + f_{\text{TBAZ}}m_{\text{TBAZ}}, \tag{16}$$

where f_{TBAZ} is the volume fraction of the TBAZ region, m_{XTL} is the rate sensitivity exponent of the crystal interior region, and m_{TBAZ} is the rate sensitivity exponent of the TBAZ region. For the ufc-Cu-control sample with the same grain size, the rate sensitivity exponent is measured to be 0.005 [6], so that $m_{\text{XTL}} = m_{\text{ufc}} = 0.005$. For the TBAZ region, the rate sensitivity exponent is assumed to be much larger than that of the crystal interior region, where we give it a value on the order of 0.085, i.e., $m_{\text{TBAZ}} = 0.085 \gg m_{\text{XTL}}$. The elasticity parameters of nt-Cu are taken to be: Young's modulus $E = 110$ GPa and Poisson's ratio $v = 0.34$.

4.1. Rate sensitivity

Fig. 5 and Table 4 summarize the modeling results including the rate sensitivity predictions using the simple
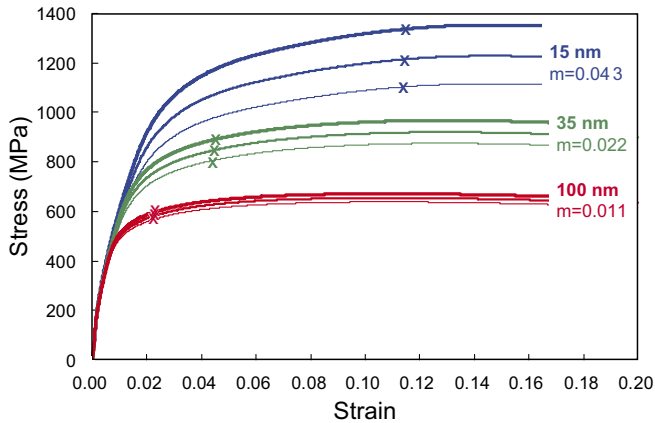
Fig. 5. Crystal plasticity simulation results. The top, middle and bottom three-curve sets show results of 15 nm (nt-Cu-fine), 35 nm (nt-Cu-medium) and 100 nm (nt-Cu-coarse) nt-Cu, respectively. The strain rates simulated are $6 \times 10^{-3}\,\mathrm{s}^{-1}$, $6 \times 10^{-2}\,\mathrm{s}^{-1}$ and $6 \times 10^{-1}\,\mathrm{s}^{-1}$, respectively. The symbol "X" denotes the predicted damage/failure initiation point.

Table 4
Summary of modeling results versus experimental data as functions of twin spacing

| | Twin spacing | | |
	15 nm	35 nm	100 nm
m (model)	0.043	0.022	0.011
m (exp, tensile)	0.037 ± 0.014	0.026 ± 0.012	0.012 ± 0.010
m (exp, jump test)	0.035–0.046	–	0.015–0.020
$\sigma_{1\%}$ (model)	838 MPa	710 MPa	552 MPa
σ_y (exp)	857 ± 50 MPa	701 ± 50 MPa	488 ± 30 MPa
$\varepsilon_{\mathrm{damage}}$ (model)	11.3%	4.5%	2.2%
$\varepsilon_{\mathrm{ts}}$ (exp)	11.6%	5.6%	2.2%
$\varepsilon_{\mathrm{failure}}$ (exp)	14%	8%	2.2%

The experimental data in this table were extracted from the stress–strain curves in Fig. 1 at the strain rate of $6 \times 10^{-3}\,\mathrm{s}^{-1}$.

rule of mixture model. The calculated values match very well with those observed experimentally.

The close matching between model prediction and experiment with respect to the size dependence of the rate sensitivity exponent also suggests that the rate sensitivity exponents of both hard mode and soft mode slip systems are increased due to the increased rate sensitivity in the TBAZ region. For example, if we only have m_{hard} or m_{soft} significantly increased, the resulting model predictions would not match so well with the experiments.

4.2. Tensile strength versus twin spacing

Fig. 5 shows the engineering stress–strain curves estimated from the crystal plasticity model through computational simulations. The experimentally observed trends in terms of flow strength and rate sensitivity versus twin lamellar spacing are both well captured by the computational model. The tensile yield strength and tensile strength both compare reasonably well with the experimental results shown in Fig. 1 and Table 1.

4.3. Deformation characteristics

Fig. 6(a) shows the nonuniform deformation within the microstructure. The nonuniform deformation is caused by two factors: (i) TB orientation within a grain and (ii) TB misalignment between adjacent grains. For example, checking the current orientation of the TBs in the deformed configuration, grains 4, 5, 6, 10, 12, 13, 14, 17, 18, 19, 23, 24, 25, 26, 33, 42, 43, 44, 47 and 52 are optimally oriented with respect to the tensile axis for soft mode shear deformation within these grains, and indeed, these grains are the most severely deformed grains in Fig. 6(a). On the other hand, a grain can be optimally oriented for soft mode deformation, but due to the "blocking" effect of its neighboring grains, it can either undergo active deformation only partially (e.g., grains 11, 42), or even exhibit a relatively low level of deformation (e.g., grain 28). The grains that are oriented with TBs nearly parallel or perpendicular to the loading axis would be forced to deform mostly with hard mode, and therefore are the least deformed grains (e.g., grains 9, 21, 29, 39, 40, 41).

Fig. 6(b) shows the map of the current local TB orientation in the deformed configuration. Within the grains (away from the boundaries), local TB slab bending can be observed frequently (e.g., in grains 13, 20, 32, 34, 35, as circled in the figure). TB bending is the result of nonuniform deformation within the microstructure, and is also frequently observed in experiments (see Fig. 2). The origin of TB bending is most likely caused by the misalignment of the TBs across different grains which results in nonuniform stress distribution and deformation.

Fig. 6(c) shows the slip direction of the most active slip system in the deformed configuration. It is clear that, for many grains that are oriented optimally for soft mode shearing, e.g., grains 6, 14, 16, 18, 19, 24, 33 and 44, the most active slip system is the soft mode with the slip direction parallel to the TBs. Nevertheless, due to the misalignment of adjacent grains and the attendant nonuniform stress distribution, activation of the hard mode shearing is abundant, especially with the grains that are oriented with TBs parallel or perpendicular to the loading axis. This shows the importance of carefully considering the effect of hard mode deformation.

Fig. 6(d) shows the distribution of lattice rotation (in degrees) within the microstructure. It is observed that grain rotations are again not uniformly distributed, with significant volume percentage reaching ± 15–$18°$. Note that in this model, no grain boundary sliding is allowed. Within individual grains, relative lattice rotation on the order of 10–$20°$ are also commonly observed within the microstructure, as shown in Fig. 6(d) as well as Fig. 6(b). This is consistent with the TEM observations (Fig. 2). The grain rotations are the natural outcome of large deformations involving crystallographic slip of the polycrystalline nt-Cu.
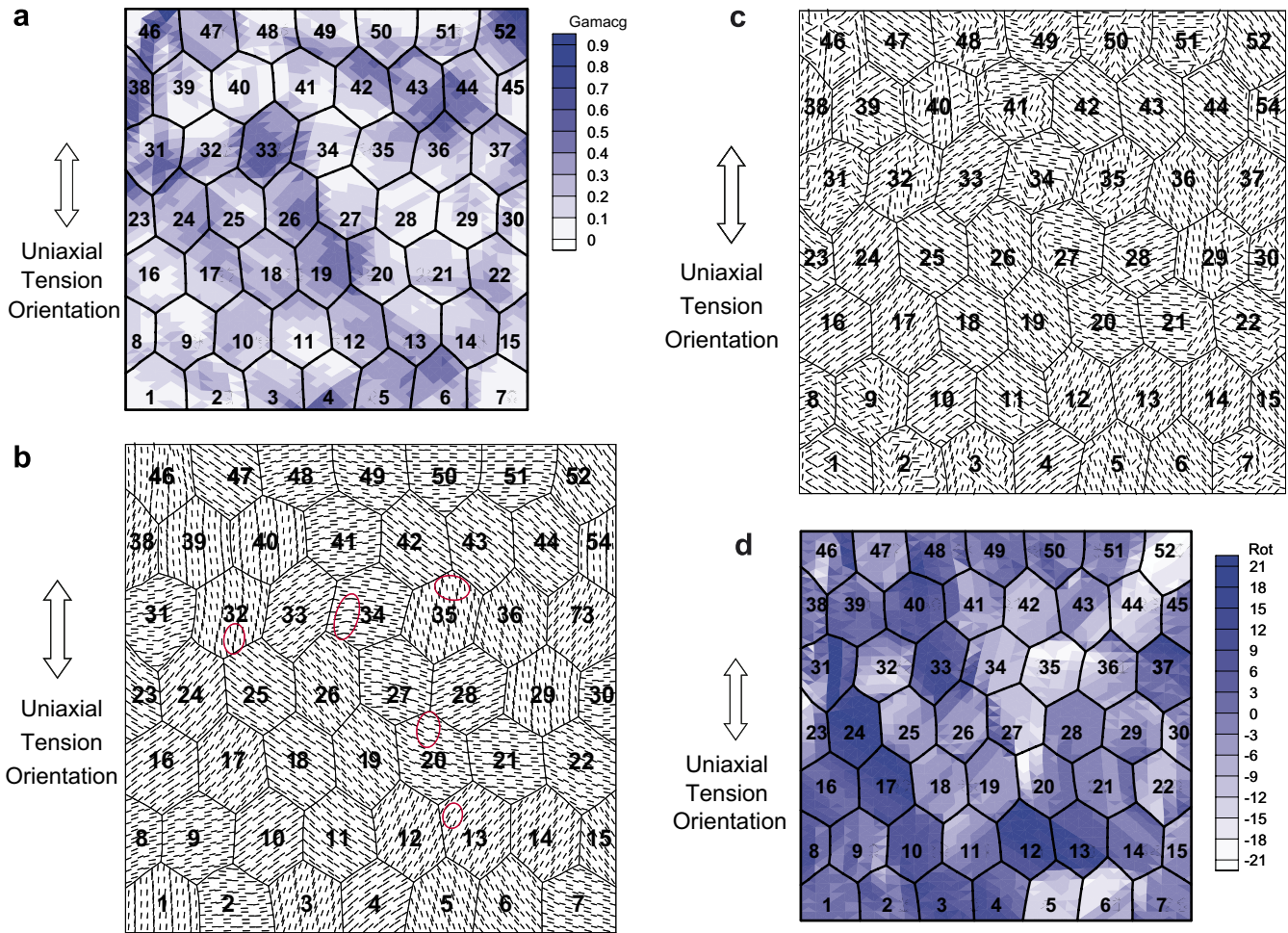
Fig. 6. Crystal plasticity simulation results. (a) Map of accumulated sum of slips; deformation is seen highly nonuniform. (b) Current TB orientation of each element; bending of TBs on the order of 15–20° is often observed in the microstructure. (c) Orientation of the currently most active slip system of each element; both hard mode and soft mode contribute to the plastic deformation. (d) Map of lattice rotation (in degrees), showing rotations on the order of ±15–18° are commonly observed in the microstructure.

5. Discussions

5.1. Nonuniform deformation and shear anisotropy

From the results shown in Fig. 6 for grains containing nanoscale twins, it is evident that the shear deformation anisotropy due to nanoscale twins results in nonuniform deformation. The soft mode deformation is mitigated by the misalignment of adjacent grains. Therefore, the interactions between many such nanoscale twin containing grains would force the activation of hard mode deformation and increase the overall flow strength of nt-Cu. The hybrid microstructure of ufc grains containing nanoscale twins is able to achieve very high strength while maintaining appreciable ductility up to 14%.

5.2. A simple criterion for ductility in nanotwinned Cu

Fig. 7 schematically shows a simple model of the twin structure for which a failure criterion as a function of twin spacing (or twin density) can be postulated. Considering

that most deformation is fairly concentrated in the vicinity of TBs (Fig. 2(b) and (c)), the idealized failure model assumes that each TB can accommodate a maximum amount of slip deformation per unit length, δ_{max}. The local maximum shear strain can thus be expressed as $\gamma_{max} = n\delta_{max}$, where n is the number of TBs per unit length (i.e., twin density). Therefore, this assumption naturally leads to the result that local ductility is directly proportional to the twin density. Taking the local ductility as $\gamma_{max} = 100\%$ at lamellar twin spacing of 15 nm, the "X" symbols in Fig. 6 show the points where local failure initiates. The failure initiation strains so predicted are likely between the ε_{ts} and $\varepsilon_{failure}$. It is seen that this model fits the experimental data shown in Fig. 1 and Table 1 very well.

From the model, we notice that the local ductility at the single crystal level is different from the global ductility due to localized deformation modes, anisotropy of slip systems and stress concentration sites. In order to develop a reasonable estimation of the ductility of nt-Cu, these factors need to be accounted for. Although the real failure process is rather complicated and all the details can not be fully
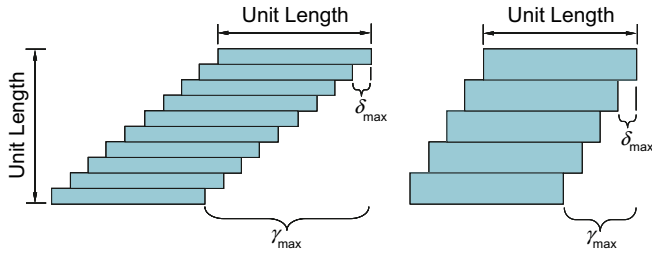
Fig. 7. Schematic drawings of a simple strain based damage/failure criterion. The model assumes that each TB can accommodate δ_{max} amount of slip deformation per unit length, i.e., $\gamma_{max} = n\delta_{max}$, where n is the number of TBs per unit length (i.e., twin density). It is clear that local ductility is directly proportional to the twin density with this assumption.
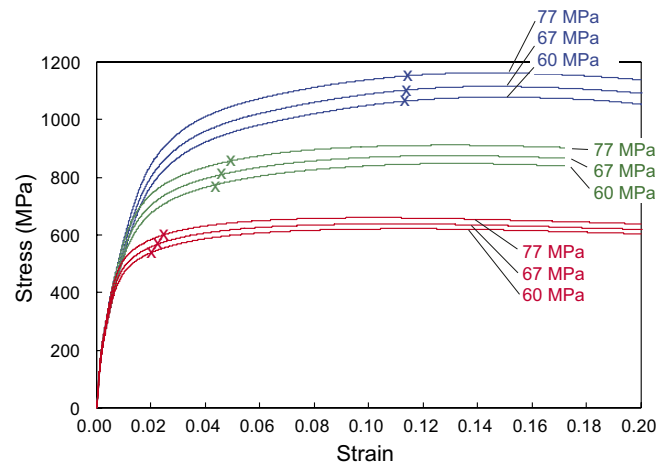

Fig. 8. Crystal plasticity simulation results obtained by varying the soft mode CRSS. The top, middle and bottom three-curve sets show results of 15 nm (nt-Cu-fine), 35 nm (nt-Cu-medium) and 100 nm (nt-Cu-coarse) nt-Cu, respectively. The soft mode CRSS values are marked in the figure. The strain rate simulated is $6 \times 10^{-3}\,\text{s}^{-1}$. The symbol "X" denotes the predicted damage/failure initiation point.

accounted for with such a simple model, this model does provide backing for the experimental result that local ductility can be regarded as being directly proportional to the twin density (when the grain size is kept constant). It is interesting to observe that, the global ductility, to the first order of approximation, can be regarded as proportional to the twin density as well.

5.3. Soft and hard mode deformation versus rate sensitivity

With a quantitative framework, we now explore possible deformation mechanisms. Specifically, does the rate sensitivity primarily arise from the soft mode deformation or hard mode deformation or both? Simulations that did not assuming both shear deformation modes to have similarly strong rate sensitivities within the TBAZ would force the model to invoke unrealistically high rate sensitivity as input in order to extract realistic mechanical property predictions. The other aspect is that the present TBAZ model is consistent with the twin density scaling of the rate sensitivity. If we take the TBAZ model assumptions, then the computational results suggest that both soft and hard shear modes need to be activated during the deformation, and furthermore the rate sensitivity of both deformation modes are increased due to the presence of TBs.

5.4. Optimization of strength and ductility versus grain size and twin spacing

Both soft mode and hard mode CRSS affect significantly the overall tensile strength of the sample. The soft mode CRSS can be controlled by grain size. This suggests that, while keeping the twin density constant, it is beneficial to reduce grain size in order to increase the overall yield strength and failure strength. Fig. 8 shows the computational engineering stress–strain curves assuming different soft mode critical resolved shear stress values, which is equivalent to varying the grain size. Increasing the soft mode critical resolved shear stress (i.e., decreasing the grain size) shows beneficial effects in terms of enhanced flow strength. However, the ductility may benefit from increasing the grain size so that along the TB there is a longer shear path.

Decreasing the grain size results in an increase in strength and a decrease in ductility, while decreasing twin spacing results in an increase in both strength and ductility. Therefore, the optimization strategy is straightforward in terms of reducing the TB spacing (provided that the nanoscale twin microstructure is still maintained). On the other hand, to achieve optimal strength, the grain size should be reduced as much as feasible (while the nanoscale twin microstructure is still maintained). Intuitively, we speculate that the ductility of nt-Cu is a decreasing function of grain size, similar to the case of polycrystalline Cu in the ultra-fine/nanocrystalline regime. The exact functional dependence of ductility versus grain size for nt-Cu is not clear at this point.

It is also worth noting here the recent atomistic reaction pathway calculations by Zhu et al. [37]. These calculations suggest that the rate-controlling mechanisms of plastic flow in nanotwinned copper could arise primarily from TB-modulated slip transfer reactions. Such reactions, in turn, would depend markedly on the dislocation density at the TBs. The relatively high ductility of nanotwinned copper occurring concomitantly with high strength would then appear to arise from the hardenability of TBs as they gradually lose coherency during mechanical deformation [37].

6. Concluding remarks

A crystal plasticity model of pure Cu containing nano-sized twins is developed based on the concept of TBAZ, where the TB is treated as a special grain boundary associated with high aspect ratio grains and special slip geometry arrangements. The model carefully takes into account possible high plastic anisotropy and rate sensitivity in nt-Cu samples. The newly developed model, with a single set of

constitutive equations/input parameters, shows reasonable agreement with experimental results for rate sensitivity, flow strength and ductility, both in terms of qualitative trends and quantitative predictions. The model provides a quantitative tool for evaluating possible optimization routes for strength and ductility.

Acknowledgements

References

[1] Koch CC, Morris DG, Lu K, Inoue A. MRS Bull 1999;24(2):54–8.
[2] Kumar KS, Van Swygenhoven H, Suresh S. Acta Mater 2003;51(19):5743–74.
[3] Schwaiger R, Moser B, Dao M, Chollacoop N, Suresh S. Acta Mater 2003;51(17):5159–72.
[4] Meyers MA, Mishra A, Benson DJ. Prog Mater Sci 2006;51(4):427–556.
[5] Ma E. JOM 2006;58(4):49–53.
[6] Christian JW, Mahajan S. Prog Mater Sci 1995;39(1–2):1–157.
[7] Lu L, Schwaiger R, Shan ZW, Dao M, Lu K, Suresh S. Acta Mater 2005;53(7):2169–79.
[8] Lu L, Shen YF, Chen XH, Qian LH, Lu K. Science 2004;304(5669):422–6.
[9] Asaro RJ, Suresh S. Acta Mater 2005;53(12):3369–82.
[10] Shen YF, Lu L, Dao M, Suresh S. Scripta Mater 2006;55(4):319–22.
[11] Schiotz J, Vegge T, Di Tolla FD, Jacobsen KW. Phys Rev B 1999;60(17):11971–83.
[12] Van Swygenhoven H, Spaczer M, Caro A, Farkas D. Phys Rev B 1999;60(1):22–5.
[13] Yamakov V, Wolf D, Phillpot SR, Gleiter H. Acta Mater 2002;50(1):61–73.
[14] Jin ZH, Gumbsch P, Ma E, Albe K, Lu K, Hahn H, et al. Scripta Mater 2006;54(6):1163–8.
[15] Hoagland RG, Kurtz RJ, Henager CH. Scripta Mater 2004;50(6):775–9.
[16] Rao SI, Hazzledine PM. Philos Mag A 2000;80(9):2011–40.
[17] Rao SI, Hazzledine PM. Scripta Mater 1999;41(10):1085–90.
[18] Wang YM, Ma E. Appl Phys Lett 2003;83(15):3165–7.
[19] Wei Q, Cheng S, Ramesh KT, Ma E. Mater Sci Eng A 2004;381(1–):71–9.
[20] Dalla Torre FH, Pereloma EV, Davies CHJ. Scripta Mater 2004;51(5):367–71.
[21] Chen J, Lu L, Lu K. Scripta Mater 2006;54(11):1913–8.
[22] Cheng S, Ma E, Wang YM, Kecskes LJ, Youssef KM, Koch CC, et al. Acta Mater 2005;53(5):1521–33.
[23] Follansbee PS, Kocks UF. Acta Metall 1988;36(1):81–93.
[24] Carrekar RP, Hibbard WR. Acta Metall 1953;1:640–63.
[25] Follansbee PS, Regazzoni G, Kocks UF. Inst Phys Conf Ser 1984;70:71–80.
[26] Mahajan S, Chin GY. Acta Metall 1973;21(2):173–9.
[27] Kumar KS, Suresh S, Chisholm MF, Horton JA, Wang P. Acta Mater 2003;51:387–405.
[28] Kad BK, Dao M, Asaro RJ. Philos Mag A 1995;71(3):567–604.
[29] Dao M, Kad BK, Asaro RJ. Philos Mag A 1996;74(3):569–91.
[30] Asaro RJ, Rice JR. J Mech Phys Solids 1977;25(5):309–38.
[31] Peirce D, Asaro RJ, Needleman A. Acta Metall 1983;31(12):1951–76.
[32] Dao M, Asaro RJ. Mech Mater 1996;23(2):103–32.
[33] Bassani JL, Wu TY. Proc Roy Soc Lond A 1991;435(1893):21–41.
[34] Cuitino AM, Ortiz M. Model Simul Mater Sci Eng 1993;1(3):225.
[35] Kalidindi SR, Schoenfeld SE. Mater Sci Eng A 2000;293(1–2):120–9.
[36] McHugh PE, Asaro RJ, Shih CF. Acta Metall 1993;41(5):1461–76.
[37] Zhu T, Li J, Samanta A, Kim HG, Suresh, S. in preparation.